universe

IMPACT FACTOR 2.9

CITESCORE 3.6

Article

Dynamics of a Cosmological Model in $f(R,T)$ Gravity: II. In Three-Dimensional Space

Jianwen Liu, Ruifang Wang and Fabao Gao

MDPI

https://doi.org/10.3390/universe9010049

universe

MDPI

Article

Dynamics of a Cosmological Model in $f(R,T)$ Gravity: II. In Three-Dimensional Space

Jianwen Liu, Ruifang Wang and Fabao Gao *

School of Mathematical Science, Yangzhou University, Yangzhou 225002, China; liuweniie@163.com (J.L.); wangruifang16@sina.com (R.W.)

* Correspondence: fbgao@yzu.edu.cn or gaofabao@sina.com

Abstract: Based on the results discussed on the invariant planes in the known literature [Universe 2022, 8, 365] for the flat FLRW space-time universe model with ideal fluid under the gravity of $f(R,T) = \xi R^{\alpha} + \zeta\sqrt{-T}$, this paper continues to describe the global dynamics of this model in the three-dimensional space containing infinity through dynamic system analysis. Moreover, the cosmological solutions of all the physical significance regions restricted by three invariant planes are also fully discussed.

Keywords: $f(R,T)$ gravity; FLRW metric; dynamic system analysis; Poincaré compactification

1. Introduction

The present Universe is flat and undergoing accelerated expansion based on recent observations [1–4]. An obscure energy termed dark energy is associated with accelerated expansion as it can generate a late-time speeding up of the cosmological foundation. The most comprehensive theory, general relativity (GR), is an excellent match with observational data. However, failing to explain the late-time acceleration [5,6], one of the shortcomings of GR, stimulates the necessity of alternative approaches to resolving the dark side puzzle. These approaches are mainly based on two methodologies. The first methodology relates to introducing a dark energy area to vary the matter substance of the Universe, starting from either a standard scalar field, a phantom field, or an amalgamation of the two fields in a unified model and then developing into more complicated scenarios [7–9]. As GR, in its usual form, may not describe the Universe's evolution accurately at astrophysical and cosmological scales, the second methodology is concerned with modifying the gravitational area. This methodology has aroused enthusiasm over the previous decades, and many novel gravity theories have been proposed. These modified gravity theories mainly incorporate $f(R)$ gravity [10,11], $f(\mathcal{T})$ gravity [12], Gauss–Bonnet gravity [13,14], $f(R,T)$ gravity [15], $f(\mathcal{T},T)$ gravity [16], and so on, where R, T, and $\mathcal{T}$ are the Ricci scalar, the trace of the energy-momentum tensor, and the torsion scalar, respectively.

As one of the simplest modified gravity theories, $f(R)$ gravity, can create a natural connection between late-time cosmic acceleration and the inflation epoch. In this gravity theory, the Ricci scalar R is substituted by an arbitrary function $f(R)$ in Einstein–Hilbert action. Hence, the field equations linked with the standard Einstein–Hilbert action get extended in $f(R)$ gravity theory. Some $f(R)$ gravity models have been tested to explain dark energy and late-time accelerated expansion [17–20]. The inflation realized by three kinds of effects, $f(R)$ gravity, the quantum anomaly, and the R^2 term in loop quantum cosmology, has been studied in [21]. Sebastiani and Myrzakulov [22] analyzed many paradigms using several revised methods and obtained effective solutions for inflation in $f(R)$ gravity. Gonzalo and Diego proposed the junction condition for $f(R)$ gravity formulated in metric-affine spaces [23] through a distributional tensor approach. It has been observed that any model in $f(R)$ gravity can be recast as a cosmological fluid in generalized Robertson–Walker space-time [24]. The latest developments in modified gravity

check for updates

Citation: Liu, J.; Wang, R.; Gao, F. Dynamics of a Cosmological Model in $f(R,T)$ Gravity: II. In Three-Dimensional Space. *Universe* **2023**, *9*, 49. https://doi.org/10.3390/universe9010049

Academic Editor: Sergei D. Odintsov

Received: 19 December 2022
Revised: 9 January 2023
Accepted: 10 January 2023
Published: 11 January 2023

and a virtual toolbox for studying inflation, dark energy, and bouncing cosmologies in the context of modified gravity have been provided in [25]. Oikonomou investigated the phenomenology of an $f(R)$ gravity model in the presence of a primordial light axion scalar field during the inflationary era [26]. The isotropization of a pre-bounce contracting phase in $f(R)$ gravity has been investigated in [27].

Another modified gravity theory named $f(R,T)$ gravity was proposed by Harko et al. in 2011 [15], which is considered as an extension of $f(R)$ gravity. This gravity theory considers the effect of a minimal coupling between matter and geometry in gravitational action. The consequence of some imperfect exotic fluid or quantum effects originating from a conformal anomaly trace may be the reason for the dependence on trace T. In $f(R,T)$ gravity theory, geometrical contributions to the total cosmic energy density and matter particles generate cosmic acceleration. After the introduction of this theory, it attracted much attention and researchers applied it to many other cosmological scenarios, including thermodynamics [28,29], redshift drift [30], wormholes [31,32], gravitational waves [33,34], baryogenesis [35], anisotropic cosmology [36], scalar perturbations [37], and Big-Bang nucleosynthesis [38]. Recently, an anisotropic version of Tolman VII isotropic solution in $f(R,T)$ gravity has been developed in [39] via the gravitational decoupling approach, where the $f(R,T)$ model proposed is fit for describing the anisotropic nature of compact stars. Shaikh [40] studied the behaviors of general relativistic hydrodynamics in the form of perfect fluid and holographic dark energy in $f(R,T)$ gravity and the obtained solutions coincide with the observations of SNe Ia and CMB. By introducing the Hubble parameter's inflation solutions, a mimetic $f(R,T)$ gravity theory in the presence of the swampland de Sitter conjecture has been analyzed in [41]. Gonçalves et al. [42] investigated the scalar-tensor representation of $f(R,T)$ gravity and inferred the explicit form of the functions $f(R,T)$. Various other studies related to $f(R,T)$ gravity can be found in [43–49].

Dynamic system analysis has been applied extensively to various models in different gravity theories [50–57] since it can depict the qualitative behavior of cosmological models where the derivation of exact solutions of evolution equations is inaccessible. Through dynamic system analysis, the dynamics of the $f(R,T) = \xi R^{\alpha} + \zeta\sqrt{-T}$ gravitational model on three invariant planes have been investigated in [57], and all the finite and infinite equilibrium points used in this work are taken from this reference. The present study mainly focuses on the dynamics of this model in three-dimensional space containing infinity, which improves the dynamic investigation of the model to a certain extent. This paper presents the dynamic behavior of the evolutionary trajectories of the cosmological model in all physically feasible regions restricted by three invariant planes and discusses the corresponding cosmological solutions.

The structure of this paper is as follows: in Section 2, we present the field equations of the model in $f(R,T)$ gravity. The dynamic equations and corresponding dynamic analysis of the model in three-dimensional space are shown in Section 3. The paper ends with a summary of the obtained results in Section 4.

2. Field Equations of $f(R,T)$ Gravity

The $f(R,T)$ gravity theory can be described by the following action

$$S = \int \sqrt{-g}d^4x\left[\frac{1}{16\pi G}f\left(R,T^{(\mathrm{m})}\right) + L^{(\mathrm{m})} + L^{(\mathrm{rad})}\right], \tag{1}$$

where G is the gravitational constant, g is the determinant of the metric, $L^{(\mathrm{m})}$ and $L^{(\mathrm{rad})}$ represent the Lagrangians of the dust matter and radiation, respectively. As usual,

$$T_{\mu\nu} \equiv -\frac{2}{\sqrt{-g}}\frac{\delta\left[\sqrt{-g}\left(L^{(\mathrm{m})} + L^{(\mathrm{rad})}\right)\right]}{\delta g^{\mu\nu}}, \tag{2}$$

Moreover, assuming that $L^{(\mathrm{m})}$ and $L^{(\mathrm{rad})}$ depend only on the metric, we obtain

$$T_{\mu\nu} = g_{\mu\nu}\left[L^{(\mathrm{m})} + L^{(\mathrm{rad})}\right] - 2\frac{\partial\left[L^{(\mathrm{m})} + L^{(\mathrm{rad})}\right]}{\partial g^{\mu\nu}}. \tag{3}$$

By considering a perfect fluid, we have

$$g^{\alpha\beta}\frac{\delta T^{(\mathrm{m})}}{\delta g^{\mu\nu}} = -2T^{(\mathrm{m})}_{\mu\nu}. \tag{4}$$

Then, by transforming the action S, the field equations become

$$\begin{aligned} f_R(R,T)R_{\mu\nu} - \frac{1}{2}f(R,T)g_{\mu\nu} + \left(g_{\mu\nu}\Box - \nabla_\mu\nabla_\nu\right)f_R(R,T) \\ = (8\pi G + f_T(R,T))T^{(\mathrm{m})}_{\mu\nu} + 8\pi G T^{(\mathrm{rad})}_{\mu\nu}, \end{aligned} \tag{5}$$

where $f_R(R,T) = \partial f(R,T)/\partial R$, $f_T(R,T) = \partial f(R,T)/\partial T$, ∇_μ denotes the covariant derivative and $\Box = \nabla^\mu\nabla_\mu$.

By contracting Equation (5), we get

$$f_R(R,T) + 3\Box f_R(R,T) - 2f(R,T) = (8\pi G + f_T(R,T))T. \tag{6}$$

Here, we are interested in studying the behavior of this theory for spatially flat FLRW space-time described by

$$ds^2 = -dt^2 + a^2(t)\left(dx^2 + dy^2 + dz^2\right), \tag{7}$$

where $a(t)$ stands for the scale factor. With the conservation of energy-momentum tensor of all matter and the relation $\nabla^\mu T^{(\mathrm{m})}_{\mu\nu} = 0 = \nabla^\mu T^{(\mathrm{rad})}_{\mu\nu}$, we find

$$\dot{f}_T(R,T) = \frac{3}{2}H(t)f_T(R,T), \tag{8}$$

where $H(t) = \dot{a}(t)/a(t)$ is the Hubble parameter, and a dot denotes the derivative with respect to the cosmic time t. With the metric (7), Equations (5) and (6) can be rewritten as

$$\begin{aligned} 3H^2 f_R(R,T) + \frac{1}{2}(f(R,T) - f_R(R,T)R) + 3H\dot{f}_R(R,T) \\ = (8\pi G + f_T(R,T))\rho^{(\mathrm{m})} + 8\pi G\rho^{(\mathrm{m})}, \end{aligned} \tag{9}$$

and

$$2\dot{H}f_R(R,T) + \ddot{f}_R(R,T) - H\dot{f}_R(R,T) = -(8\pi G + f_T(R,T))\rho^{(\mathrm{m})} - \frac{32}{3}\pi G\rho^{(\mathrm{rad})}. \tag{10}$$

3. Dynamic Analysis of the $f(R,T) = \xi R^\alpha + \zeta\sqrt{-T}$ Model

3.1. Dynamic Equations

In this section, we consider the minimally coupled $f(R,T)$ gravity, i.e., $f(R,T) = g(R) + h(T)$. In order to obtain the dynamic equations, we introduce six dimensionless independent variables [49], namely,

$$x_1 \equiv -\frac{\dot{g}'(R)}{Hg'(R)}, x_2 \equiv -\frac{g(R)}{6H^2g'(R)}, x_3 \equiv \frac{R}{6H^2} = \frac{\dot{H}}{H^2} + 2, \tag{11}$$

$$x_4 \equiv -\frac{h(T)}{3H^2g'(R)}, x_5 \equiv -\frac{8\pi G\rho^{(\mathrm{rad})}}{3H^2g'(R)}, x_6 \equiv -\frac{Th'(T)}{3H^2g'(R)}. \tag{12}$$

We also define four dimensionless parameters [49] as follows

$$m \equiv \frac{Rg''(R)}{g'(R)}, r \equiv -\frac{Rg'(R)}{g(R)} = \frac{x_3}{x_2}, n \equiv \frac{Th''(T)}{h'(T)}, s \equiv \frac{Th'(T)}{h(T)} = \frac{x_6}{x_4}. \tag{13}$$

We can rewrite Equations (9) and (10) as

$$1 + \frac{g}{6H^2g'} + \frac{h}{6H^2g'} - \frac{R}{6H^2} + \frac{\dot{g}'}{Hg'} = \frac{8\pi G\rho^{(\mathrm{m})}}{3H^2g'} + \frac{h'\rho^{(\mathrm{m})}}{3H^2g'} + \frac{8\pi G\rho^{(\mathrm{rad})}}{3H^2g'}, \tag{14}$$

and

$$2\frac{\dot{H}}{H^2} + \frac{\ddot{g}'}{H^2g'} - \frac{\dot{g}'}{Hg'} = -\frac{8\pi G\rho^{(\mathrm{m})}}{H^2g'} - \frac{h'\rho^{(\mathrm{m})}}{H^2g'} - \frac{32\pi G\rho^{(\mathrm{rad})}}{3H^2g'}. \tag{15}$$

Equation (8) becomes

$$Th'' = -\frac{1}{2}h', \tag{16}$$

and then we get

$$Th' - \frac{1}{2}h + C = 0, \tag{17}$$

where C is an integration constant. Set $C = 0$, which leads to $s = 1/2$. Then, we obtain $x_4 = 2x_6$ and $h = \zeta\sqrt{-T}$, where ζ is a constant.

We study the late-time behaviors of this model, i.e., radiation does not exist, and consider the form $f(R,T) = \xi R^{\alpha} + \zeta\sqrt{-T}$, where ξ is a constant. Thus, we get

$$x_3 = -\alpha x_2, m = \alpha - 1. \tag{18}$$

Setting $x_1 \equiv x, x_2 \equiv y, x_4 \equiv z$, we obtain the autonomous dynamic system

$$\begin{aligned} \frac{dx}{dN} &= -1 + x(x + \alpha y) + (\alpha - 3)y - \frac{3}{2}z, \\ \frac{dy}{dN} &= -\frac{xy}{\alpha - 1} + 2y(2 + \alpha y), \\ \frac{dz}{dN} &= z\left(\frac{5}{2} + x + 2\alpha y\right), \end{aligned} \tag{19}$$

where $N = \ln a$. The density parameter of matter $\Omega^{(\mathrm{m})}$ and effective equation of state $\omega^{(\mathrm{eff})}$ are defined as follows

$$\Omega^{(\mathrm{m})} \equiv \frac{8\pi G\rho^{(\mathrm{m})}}{3H^2g'} = 1 - x + (\alpha - 1)y - z, \tag{20}$$

$$\omega^{(\mathrm{eff})} \equiv -1 - \frac{2\dot{H}}{3H^2} = \frac{1}{3}(1 + 2\alpha y). \tag{21}$$

3.2. Dynamic Analysis in Three-Dimensional Space

Dynamic analysis of system (19) on invariant planes has been presented in [57], where the equilibrium points used in the following are provided. According to [57], the cosmological solution matching observations can be obtained when $\alpha > 1$ and α is approaching 1. Here, we set $\alpha = 1.1$ to proceed with the dynamic analysis of the system in 3D. Other values of α can be taken to study this model similarly. The finite equilibrium points of system (19) are summarized in Table 1.

From Table 1, the points p_1, p_3 are radiation points with $\Omega^{(\mathrm{m})} = 0$ and $\omega^{(\mathrm{eff})} = 1/3$. The eigenvalues of p_1, p_3 are $7/2$, 2, -6 and $-7/2$, $-3/2$, 9, respectively, so these points are saddles.

The point p_2 can be considered as a ϕ-matter-dominated epoch (ϕMDE) [58] with $\Omega^{(\mathrm{m})} = 2$ and $\omega^{(\mathrm{eff})} = 1/3$. Although the value of the matter-density parameter does not match the effective equation of state, the Universe's evolution may be related to this point in the model. The eigenvalues of p_2 are $3/2, -2, 14$, so p_2 is a saddle.

For point p_4, it has $\Omega^{(\mathrm{m})} = 0$ and $\omega^{(\mathrm{eff})} = 4$. As this point cannot describe any known matter, we consider it nonphysical. The eigenvalues of p_4 are $27/2, 6, 5/4$, so p_4 is unstable.

The equilibrium point p_5 can present a matter-dominated era with $\Omega^{(\mathrm{m})} = 81/121$ and $\omega^{(\mathrm{eff})} = -1/10$. The eigenvalues of p_5 are $3/2, -15/22 \pm \beta \mathrm{i}$, where $\beta \approx 2.9845$ and $\mathrm{i}^2 = -1$, so p_5 is unstable.

The point p_6 can be used to explain the late accelerating expansion of the Universe. At this point, matter and radiation are absent, while the Universe is dominated by dark energy. This point has $\Omega^{(\mathrm{m})} = 0$ and $\omega^{(\mathrm{eff})} = -6/11$. The eigenvalues of p_6 are $3/2, -12/11 \pm \gamma \mathrm{i}$, where $\gamma \approx 4.5144$, so p_6 is a stable spiral point.

For the infinite equilibrium points e_{13}, E_{13}, and a set of non-isolated points filling up the circle where the plane $y = 0$ intersects the Poincaré sphere, we can only describe the trend of the trajectories around them. Because the coordinates of these infinite points are indistinct, it is challenging to study their physical properties.

Table 1. The finite equilibrium points of the dynamical systems.

Point	Coordinates	Scale Factor	$\Omega^{(\mathrm{m})}$	$\omega^{(\mathrm{eff})}$	Stability
p_1	$(1,0,0)$	$a(t) = a_0\left(\frac{t-t_i}{t_0-t_i}\right)^{\frac{1}{2}}$	0	$\frac{1}{3}$	saddle
p_2	$(-1,0,0)$	$a(t) = a_0\left(\frac{t-t_i}{t_0-t_i}\right)^{\frac{1}{2}}$	2	$\frac{1}{3}$	saddle
p_3	$(-\frac{5}{2},0,\frac{7}{2})$	$a(t) = a_0\left(\frac{t-t_i}{t_0-t_i}\right)^{\frac{1}{2}}$	0	$\frac{1}{3}$	saddle
p_4	$(\frac{3}{2},5,0)$	$a(t) = a_0\left(\frac{t-t_i}{t_0-t_i}\right)^{\frac{2}{15}}$	0	4	unstable
p_5	$(\frac{3}{11},\frac{70}{121},0)$	$a(t) = a_0\left(\frac{t-t_i}{t_0-t_i}\right)^{\frac{11}{15}}$	$\frac{81}{121}$	$-\frac{1}{10}$	unstable
p_6	$(\frac{3}{22},-\frac{145}{121},\frac{90}{121})$	$a(t) = a_0\left(\frac{t-t_i}{t_0-t_i}\right)^{\frac{22}{15}}$	0	$-\frac{6}{11}$	stable

The three planes $y = 0$, $z = 0$ and $\Omega^{(\mathrm{m})} = 0$ are invariant planes of system (19). Through Poincaré compactification [59], the infinite space can be closed to the finite, so the whole space can be regarded as a Poincaré ball. A Poincaré ball is divided by these three invariant planes into eight regions R_i $(i = 1, \cdots, 8)$, as shown in Figure 1. The accurate representation of regions R_i $(i = 1, \cdots, 8)$ is

$$\begin{aligned}
&\mathrm{R}_1 : x < 0,\ \Omega^{(\mathrm{m})} > 0,\ z > 0, \quad \mathrm{R}_2 : x > 0,\ \Omega^{(\mathrm{m})} > 0,\ z > 0,\\
&\mathrm{R}_3 : x < 0,\ \Omega^{(\mathrm{m})} > 0,\ z < 0, \quad \mathrm{R}_4 : x > 0,\ \Omega^{(\mathrm{m})} > 0,\ z < 0,\\
&\mathrm{R}_5 : x < 0,\ \Omega^{(\mathrm{m})} < 0,\ z > 0, \quad \mathrm{R}_6 : x > 0,\ \Omega^{(\mathrm{m})} < 0,\ z > 0,\\
&\mathrm{R}_7 : x < 0,\ \Omega^{(\mathrm{m})} < 0,\ z < 0, \quad \mathrm{R}_8 : x > 0,\ \Omega^{(\mathrm{m})} < 0,\ z < 0.
\end{aligned}$$

The cosmological solutions in the viable $f(R)$ gravity models hold $g'(R) > 0$ which guarantees that gravity is an attractive force. According to the definition of $\Omega^{(\mathrm{m})}$, these solutions must have $\Omega^{(\mathrm{m})} \geq 0$. The condition $\Omega^{(\mathrm{m})} \geq 0$ should hold in this model because $f(R)$ gravity can be considered as a particular case of $f(R,T) = g(R) + h(T)$ gravity with $h(T) = 0$. From Figure 1, we know that $\Omega^{(\mathrm{m})} > 0$ in regions R_i $(i = 1,2,3,4)$, $\Omega^{(\mathrm{m})} < 0$ in regions R_i $(i = 5,6,7,8)$. Thus, we will focus on the dynamics of regions R_i $(i = 1,2,3,4)$ instead of R_i $(i = 5,6,7,8)$.

The dynamic behavior of system (19) inside regions R_i $(i = 1, 2, 3, 4)$ is determined by the following five planes and one surface, which divide these four regions into several subregions:

$$y = 0, \quad z = 0, \quad \Omega^{(m)}(x, y, z) = 0,$$
$$b_1(x, y, z) = 0, \quad b_2(x, y) = 0, \quad b_3(x, y) = 0,$$

where

$$\Omega^{(m)}(x, y, z) = 1 - x + 0.1y - z,$$
$$b_1(x, y, z) = -1 + x^2 + 1.1xy - 1.9y - 1.5z,$$
$$b_2(x, y) = -10x + 2.2y + 4,$$
$$b_3(x, y) = x + 2.2y + 2.5.$$

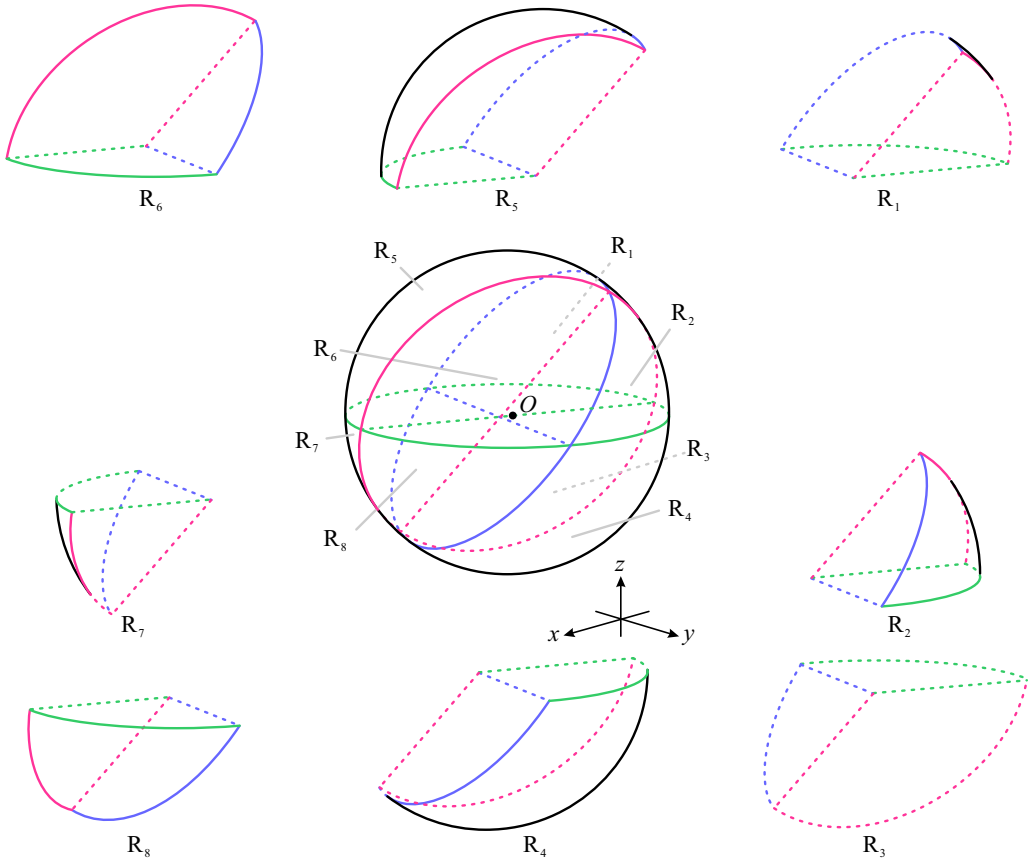

Figure 1. The Poincaré ball is divided into eight regions. The green plane is $z = 0$, the blue plane is $\Omega^{(m)} = 0$, the pink plane is $y = 0$ and a set of non-isolated equilibrium points fill up the pink circle where the plane $y = 0$ intersects Poincaré sphere. The point O is the center of the ball.

The region R_1 is divided into seven subregions R_{1i} $(i = 1, \cdots, 7)$ (see Figures 2 and 3). The dynamic behavior of system (19) in these seven subregions is presented in Table 2.

For subregion R_{11}, its front part is bounded by $\Omega^{(m)} = 0$ and $y = 0$, its back is restricted by the Poincaré sphere, and its bottom is limited in $z = 0$. As shown in Table 2, the trajectories of system (19) monotonically decrease in the positive y and z axes and increase in the positive x axis, which indicates that the trajectories in R_{11} can get to subregions R_{12}, R_{17} and the sources of these trajectories are subregion R_{16} and infinite equilibrium points in $y = 0$ restricted to R_{11}.

The right of subregion R_{12} is restricted by Poincaré sphere, the left is limited by $b_3 = 0$, the back is bounded by $\Omega^{(m)} = 0$, the bottom is confined by $z = 0$ and the front is bounded by $b_2 = 0$. The movement of trajectories in R_{12} increases monotonically in the positive x and y axes, and decreases in the positive z axis. Thus, R_{11} is the source of these trajectories and R_{13} is the subregion that these trajectories tend to.

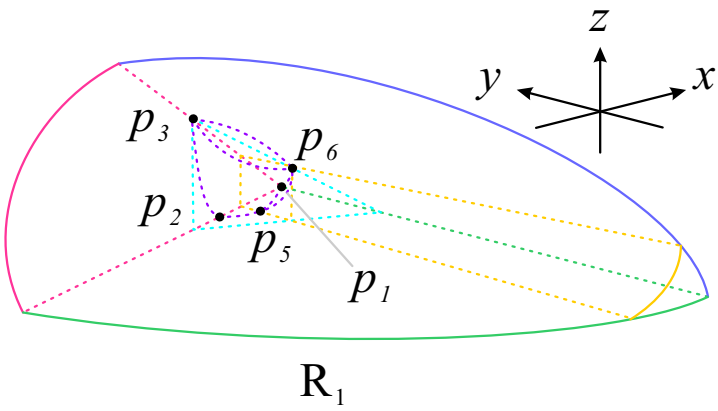

Figure 2. The purple surface is $b_1 = 0$, the yellow plane is $b_2 = 0$, and the light blue plane is $b_3 = 0$.

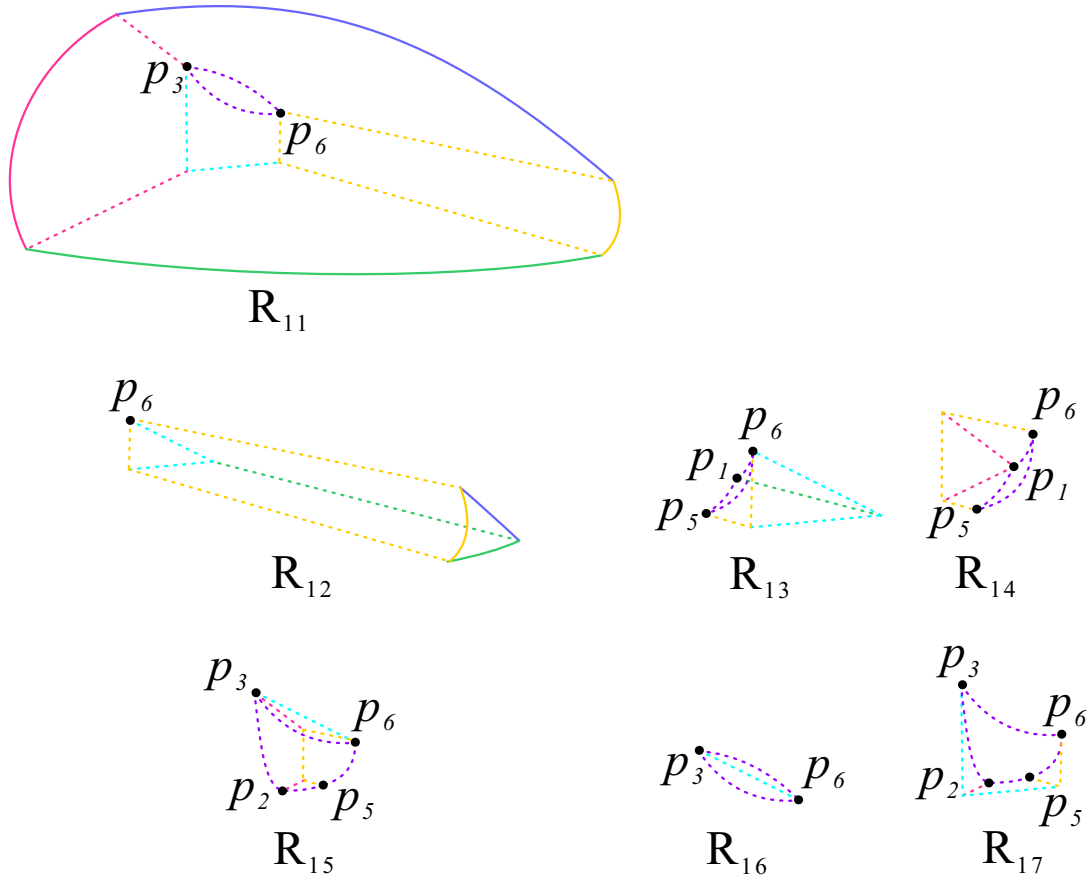

Figure 3. The region R_1 is divided into seven subregions by the five planes $y = 0$, $z = 0$, $\Omega^{(m)} = 0$, $b_2 = 0$, and $b_3 = 0$, and one surface $b_1 = 0$.

Table 2. Dynamic behavior of the trajectories in the seven subregions.

Subregion	Corresponding Region	Dynamic Behavior
R_{11}	$b_1 > 0, b_2 > 0, b_3 < 0, y < 0, z > 0$	$\dot{x} > 0, \dot{y} < 0, \dot{z} < 0$
R_{12}	$b_1 > 0, b_2 < 0, b_3 < 0, y < 0, z > 0$	$\dot{x} > 0, \dot{y} > 0, \dot{z} < 0$
R_{13}	$b_1 > 0, b_2 < 0, b_3 > 0, y < 0, z > 0$	$\dot{x} > 0, \dot{y} > 0, \dot{z} > 0$
R_{14}	$h_1 < 0, h_2 < 0, h_3 > 0, y < 0, z > 0$	$\dot{x} < 0, \dot{y} > 0, \dot{z} > 0$
R_{15}	$b_1 < 0, b_2 > 0, b_3 > 0, y < 0, z > 0$	$\dot{x} < 0, \dot{y} < 0, \dot{z} > 0$
R_{16}	$b_1 < 0, b_2 > 0, b_3 < 0, y < 0, z > 0$	$\dot{x} < 0, \dot{y} < 0, \dot{z} < 0$
R_{17}	$b_1 > 0, b_2 > 0, b_3 > 0, y < 0, z > 0$	$\dot{x} > 0, \dot{y} < 0, \dot{z} > 0$

The right side of R_{13} is restricted by $b_3 = 0$, its left is confined by $b_1 = 0$, and its front, bottom, and back parts are limited by the planes $b_2 = 0$, $z = 0$, and $\Omega^{(m)} = 0$, respectively. The tendency of trajectories in subregion R_{13} presents a monotone increase along the positive three axes. The trajectories in R_{13} originate from subregions R_{12}, R_{17}, and the point p_5, and then move to R_{14} and p_6.

For subregion R_{14}, its front and back are bounded by b_2 and $\Omega^{(m)} = 0$, respectively, its bottom is limited by $z = 0$, and its left and right are restricted by $y = 0$ and $b_1 = 0$, respectively. The trajectories in R_{14} monotonically decrease in the positive x axis, increase in the positive y and z axes, so the trajectories are from R_{13} and go to R_{15}.

The front part of subregion R_{15} is restricted by $b_1 = 0$, the back is bounded by $y = 0$ and $b_3 = 0$, the upper is limited by $\Omega^{(m)} = 0$ and $b_3 = 0$, and the bottom is confined by $z = 0$. In subregion R_{15}, trajectories are monotone decreasing in the positive x and z axes while increasing in the positive y axis. Therefore, these trajectories are from R_{14} and move to R_{16}.

For R_{16}, its front part is bounded by $b_3 = 0$ and its back part is confined by two planes $\Omega^{(m)} = 0$ and $b_3 = 0$. The behavior of trajectories in this subregion is decreasing monotonically in the positive three axes, so these trajectories stem from p_3 and R_{15} and then enter into R_{11}.

The back, left, right, lower, and front parts of subregion R_{17} are bounded by the surface $b_1 = 0$, the planes $b_3 = 0$, $y = 0$, $b_2 = 0$, and $z = 0$, respectively. The trajectories in R_{17} monotonically decrease in the positive y axis and increase in the positive x and z axes. Hence, they come from subregions R_{11}, R_{15}, and the point p_5 and move towards p_6.

Overall, the dynamic behavior of the trajectories in the seven subregions of R_1 analyzed above can be displayed as

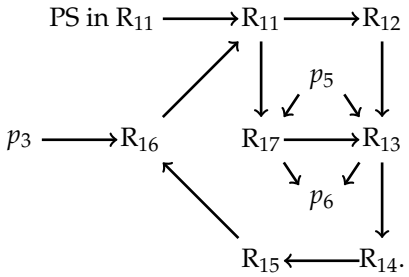

Note: PS is a Poincaré sphere.

According to the process of dynamics represented above, the trajectories of system (19) in the region R_1 possess an ω-limit, i.e., future attractor, at p_6 and α-limits, i.e., past attractor, at the infinite equilibrium points in $y = 0$ limited to R_{11} and the finite equilibrium points p_3, p_5. Although the points p_3 and p_5 have positive real eigenvalues, they are post attractors in R_1. Cosmological solutions matching observations go through a long enough matter-dominated epoch and then into an accelerated expansion, i.e., an unstable point of

matter switches to a stable acceleration equilibrium point in phase space. The trajectories originated from p_5 can get to p_6 through subregions R_{13} or R_{17}, which represent a class of cosmological solutions.

The region R_2 is divided into five subregions R_{2i} $(i = 1, \cdots, 5)$, shown in Figures 4 and 5, and Table 3 displays the dynamic behavior of system (19) in these five subregions.

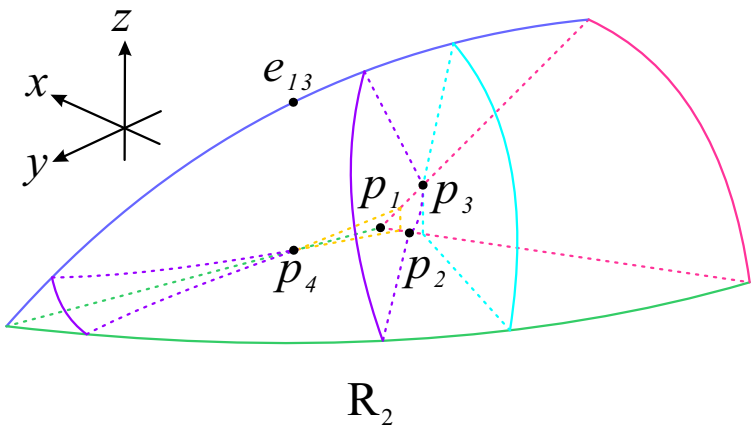

Figure 4. The purple surface is $b_1 = 0$, the yellow plane is $b_2 = 0$, and the light blue plane is $b_3 = 0$.

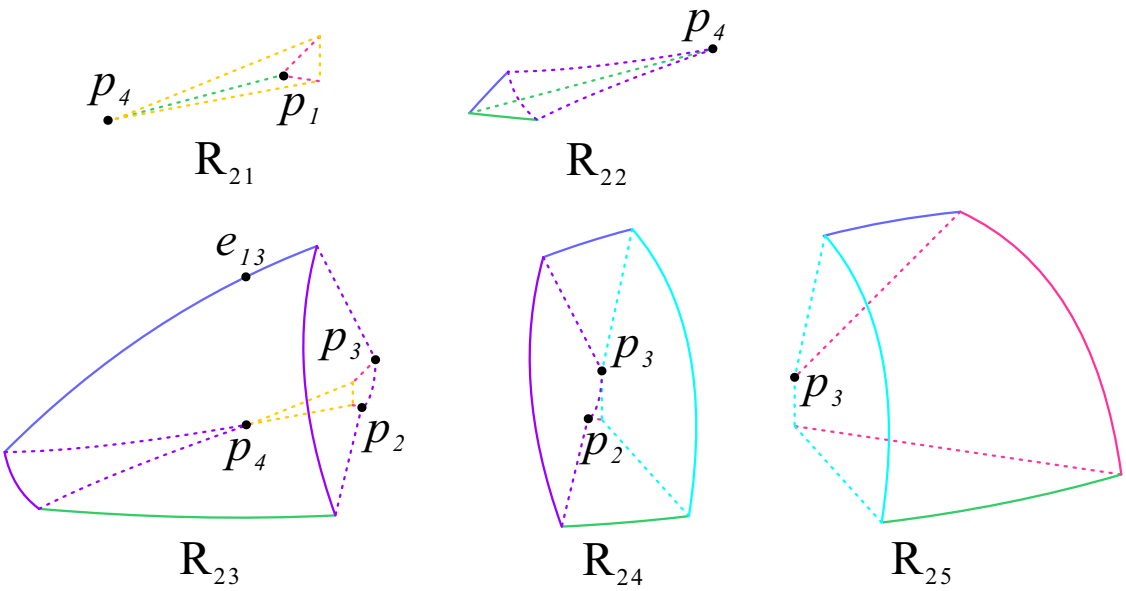

Figure 5. The region R_2 is divided into five subregions by the five planes $y = 0$, $z = 0$, $\Omega^{(m)} = 0$, $b_2 = 0$, and $b_3 = 0$, and one surface $b_1 = 0$.

Table 3. Dynamic behavior of the trajectories in the five subregions.

Subregion	Corresponding Region	Dynamic Behavior
R_{21}	$b_1 < 0, b_2 < 0, b_3 > 0, y > 0, z > 0$	$\dot{x} < 0, \dot{y} < 0, \dot{z} > 0$
R_{22}	$b_1 > 0, b_2 > 0, b_3 > 0, y > 0, z > 0$	$\dot{x} > 0, \dot{y} > 0, \dot{z} > 0$
R_{23}	$b_1 < 0, b_2 > 0, b_3 > 0, y > 0, z > 0$	$\dot{x} < 0, \dot{y} > 0, \dot{z} > 0$
R_{24}	$b_1 > 0, b_2 > 0, b_3 > 0, y > 0, z > 0$	$\dot{x} > 0, \dot{y} > 0, \dot{z} > 0$
R_{25}	$b_1 > 0, b_2 > 0, b_3 < 0, y > 0, z > 0$	$\dot{x} > 0, \dot{y} > 0, \dot{z} < 0$

As shown in Figure 5, the front of subregion R_{21} is bounded by the plane $b_2 = 0$, the back is limited by $\Omega^{(m)} = 0$, the base is restricted by $z = 0$, and the right is confined by $y = 0$. The trajectories of system (19) in R_{21} decrease monotonically in the positive x and y axes and increase in the positive z axis. Accordingly, the trajectories in R_{21} are from p_4 and go to R_{23}.

For subregion R_{22}, its front part is restricted by Poincaré sphere and $b_1 = 0$, its back is bounded by $\Omega^{(m)} = 0$, and its bottom is confined by $z = 0$. In this subregion, the trajectories of system (19) increase monotonically in the positive three axes directions. Therefore, these trajectories originate from p_4 and get to R_{23}.

The front of subregion R_{23} is bounded by the Poincaré sphere, the back is limited by $y = 0$ and $b_2 = 0$, the left and right are limited by $b_1 = 0$, and the bottom is confined by $z = 0$. In R_{23}, the trajectories are monotone decreasing in the positive y and z axes and increasing in the positive x axis, which shows that these trajectories can get to e_{13} and the sources of them are p_2, p_3, p_4, R_{21}, R_{22}, and R_{24}.

The front of subregion R_{24} is restricted by Poincaré sphere, the left is confined by the surface $b_1 = 0$, and the right, the upper, and the lower are limited by the planes $b_3 = 0$, $\Omega^{(m)} = 0$, and $z = 0$, respectively. The trajectories in R_{24} behave the same as those in subregion R_{22}. Thus, they come from R_{25} and leave for R_{23}.

The front of R_{25} is restricted by Poincaré sphere and $b_3 = 0$, the back is limited by $y = 0$, the upper is confined by $\Omega^{(m)} = 0$, and the lower is bounded by $z = 0$. The tendency of the trajectories in this subregion displays a monotonic increase in the positive x and y axes, and a monotonic decrease in the positive z axis. The trajectories thereby originate from infinite equilibrium points in $y = 0$ restricted to R_{25} and point to R_{24}.

In summary, the dynamic behavior of the trajectories in the five subregions of R_2 discussed above is shown below.

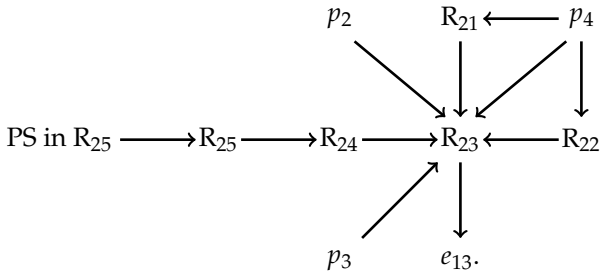

From the dynamic demonstration of R_2, we find that the trajectories in R_2 own an ω-limit at e_{13} and α-limits at infinite equilibrium points in $y = 0$ limited to R_{25} and finite equilibrium points p_2, p_3, p_4. In addition, p_4 is a past attractor for its instability. We find that there are trajectories that originate from p_2, p_3, p_4 and infinite point in $y = 0$ restricted by R_{25} and move to e_{13} in the region R_2. However, cosmological solutions can not be found in this region.

The region R_3 is divided into seven subregions R_{3i} $(i = 1, \cdots, 7)$ (see Figures 6 and 7). The dynamic behavior of the system (19) in these seven subregions is presented in Table 4.

In Figure 7, the right side of the subregion is limited by the plane $y = 0$ and the left is restricted by $b_2 = 0$, the front part of R_{31} is bounded by Poincaré sphere, the back is confined by $b_3 = 0$ and the top is restricted by $z = 0$. As shown in Table 3, the trajectories of system (19) in subregion R_{31} are monotone increasing in the positive x and z axes, decreasing in the positive y axis. Therefore, the trajectories in R_{31} stem from the infinite equilibrium points in $y = 0$ restricted to R_{31} and get into subregions R_{32} and R_{36}.

The bottom of subregion R_{32} is restricted by the Poincaré sphere, the top is limited by $z = 0$ and $b_1 = 0$, the front is bounded by $b_3 = 0$ and the back is confined by $y = 0$ and $h_2 = 0$. The behavior of trajectories in R_{32} is the same with those in subregion R_{31}. For this reason, the trajectories in this subregion derive from R_{31} and R_{33}, then enter R_{35}.

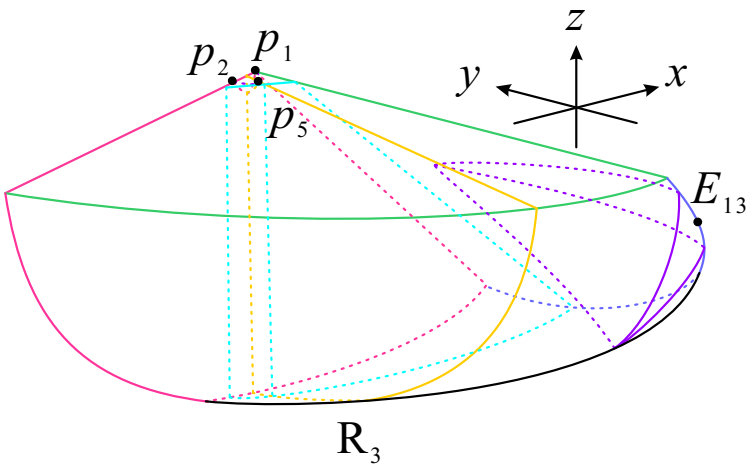

Figure 6. The purple surface is $b_1 = 0$, the yellow plane is $b_2 = 0$, and the light blue plane is $b_3 = 0$.

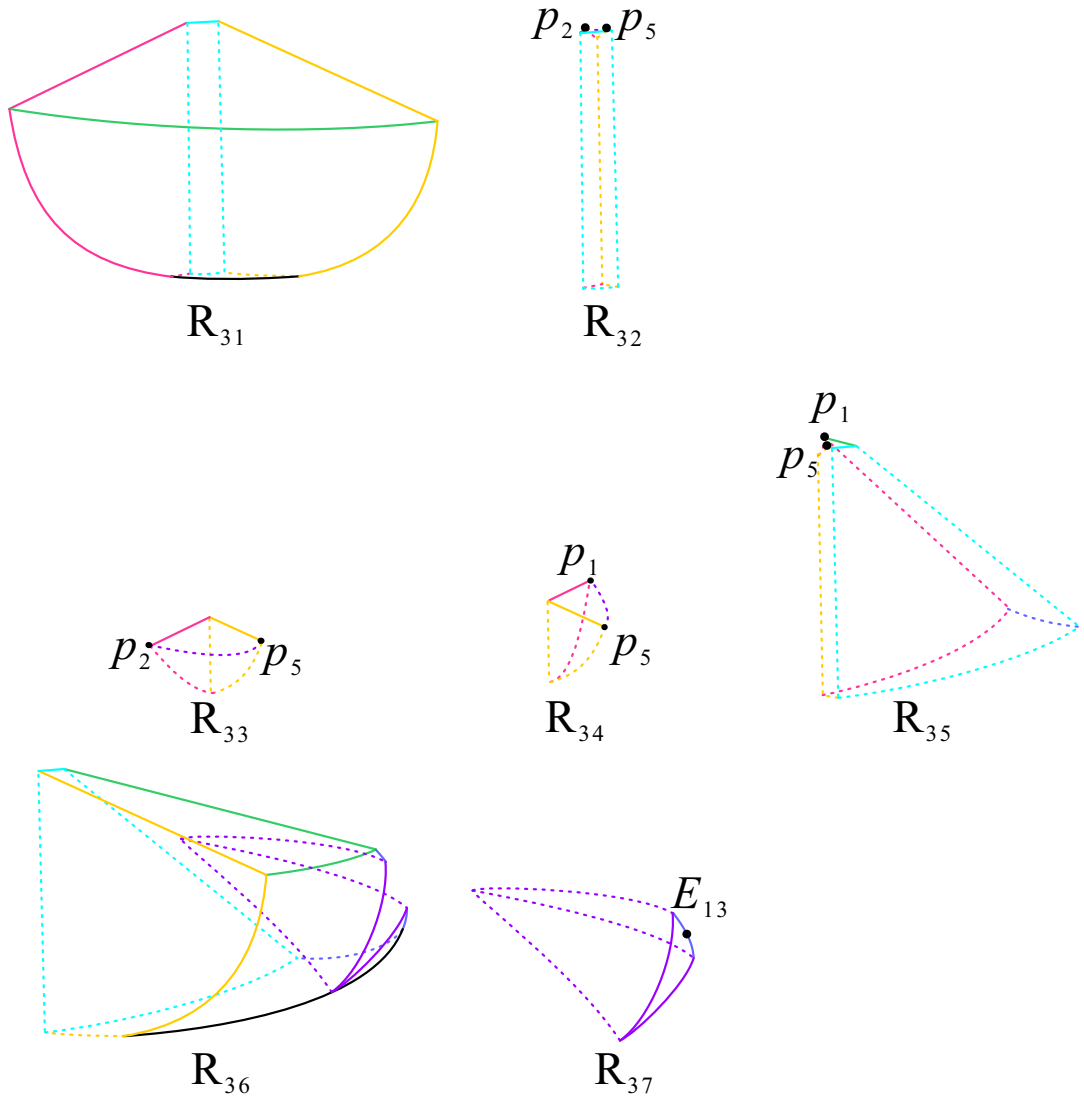

Figure 7. The region R_3 is divided into seven subregions by the five planes $y = 0$, $z = 0$, $\Omega^{(m)} = 0$, $b_2 = 0$, and $b_3 = 0$, and one surface $b_1 = 0$.

Table 4. Dynamic behavior of the trajectories in the seven subregions.

Subregion	Corresponding Region	Dynamic Behavior
R_{31}	$b_1 > 0, b_2 > 0, b_3 < 0, y < 0, z < 0$	$\dot{x} > 0, \dot{y} < 0, \dot{z} > 0$
R_{32}	$b_1 > 0, b_2 > 0, b_3 > 0, y < 0, z < 0$	$\dot{x} > 0, \dot{y} < 0, \dot{z} < 0$
R_{33}	$b_1 < 0, b_2 > 0, b_3 > 0, y < 0, z < 0$	$\dot{x} < 0, \dot{y} < 0, \dot{z} < 0$
R_{34}	$b_1 < 0, b_2 < 0, b_3 > 0, y < 0, z < 0$	$\dot{x} < 0, \dot{y} > 0, \dot{z} < 0$
R_{35}	$b_1 > 0, b_2 < 0, b_3 > 0, y < 0, z < 0$	$\dot{x} > 0, \dot{y} > 0, \dot{z} < 0$
R_{36}	$b_1 > 0, b_2 < 0, b_3 < 0, y < 0, z < 0$	$\dot{x} > 0, \dot{y} > 0, \dot{z} > 0$
R_{37}	$b_1 < 0, b_2 < 0, b_3 < 0, y < 0, z < 0$	$\dot{x} < 0, \dot{y} > 0, \dot{z} > 0$

For subregion R_{33}, its front part is bounded by $b_1 = 0$, its back is restricted by $y = 0$ and $b_2 = 0$, and the top is limited by $z = 0$. In R_{33}, the trajectories are monotone decreasing in the positive three axes, which shows that the source of the trajectories in R_{33} is R_{34} and these trajectories then go into R_{32}.

The front part of subregion R_{34} is restricted by $b_2 = 0$, the upper is bounded by $z = 0$, and the back is limited by $y = 0$ and h_1. The tendency of trajectories in R_{34} is monotonic increasing in the positive y axis and decreasing in the positive x and z axes. Thus, the trajectories in this subregion originate from p_5 and leave for R_{33}.

The upper part of subregion R_{35} is restricted by $z = 0$ and $b_1 = 0$, the left and the right are limited by $b_2 = 0$ and $\Omega^{(m)} = 0$, respectively, and the front and the back are confined by $b_3 = 0$ and $y = 0$, respectively. In subregion R_{35}, the trajectories monotonically increase in the positive x and y axes, decrease in the positive z axis, which points that they come from R_{32} and R_{36}, then leave for the infinite equilibrium points in $y = 0$ limited to R_{35}.

For R_{36}, its front part is limited by $b_2 = 0$ and the Poincaré sphere, its top is bounded by $z = 0$, and its back is restricted by $b_3 = 0$, $\Omega^{(m)} = 0$ and $b_1 = 0$. In R_{36}, the dynamic behavior of trajectories is monotone increasing in positive three axes. The trajectories in this subregion are from R_{37} and move to R_{35}.

The right part of R_{37} is bounded by Poincaré sphere, the back is limited by $\Omega^{(m)} = 0$, and other parts are restricted by $b_1 = 0$. The behavior of the trajectories in R_{37} shows a monotonic decrease in the positive x and z axes and increases in the positive y axis. For this reason, the trajectories in R_{37} originate from the infinite equilibrium point E_{13} and go to R_{36}.

On the whole, the behavior of the trajectories in the seven subregions of R_3 discussed above can be described as

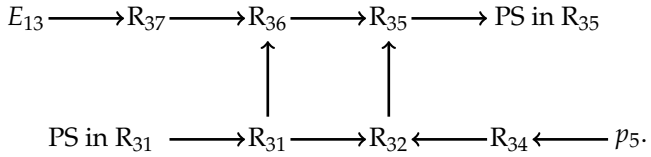

The dynamic process above indicates that the trajectories in R_3 possess ω-limits at the infinite equilibrium points in $y = 0$ restricted to R_{35} and α-limits at E_{13} and the infinite equilibrium points in $y = 0$ restricted to R_{31}. We find that trajectories originating from p_5 can reach the infinite equilibrium points in $y = 0$ limited to R_{35}. However, this region contains no cosmological solutions because the infinite points that the trajectories point to are not accelerated stable points.

The region R_4 is divided into five subregions R_{4i} $(i = 1, \cdots, 5)$, as shown in Figures 8 and 9. The dynamic behavior of system (19) in these five subregions is displayed in Table 5.

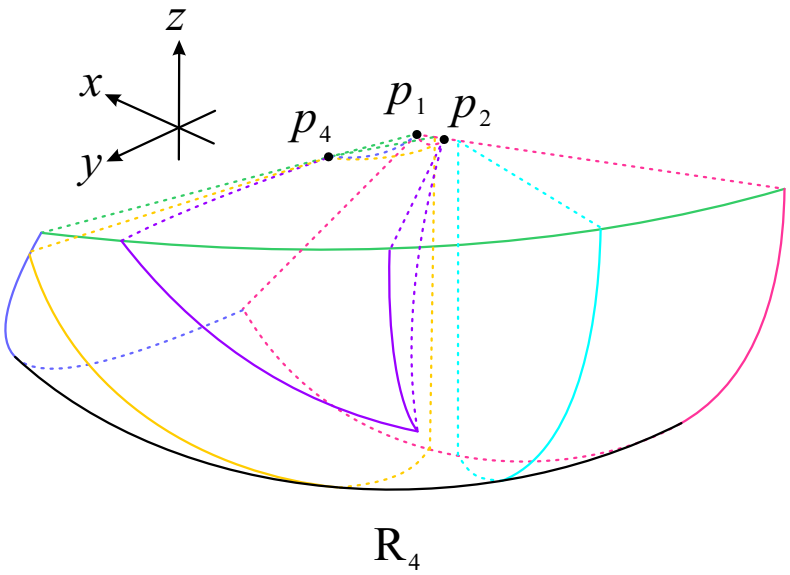

Figure 8. The purple surface is $b_1 = 0$, the yellow plane is $b_2 = 0$, and the light blue plane is $b_3 = 0$.

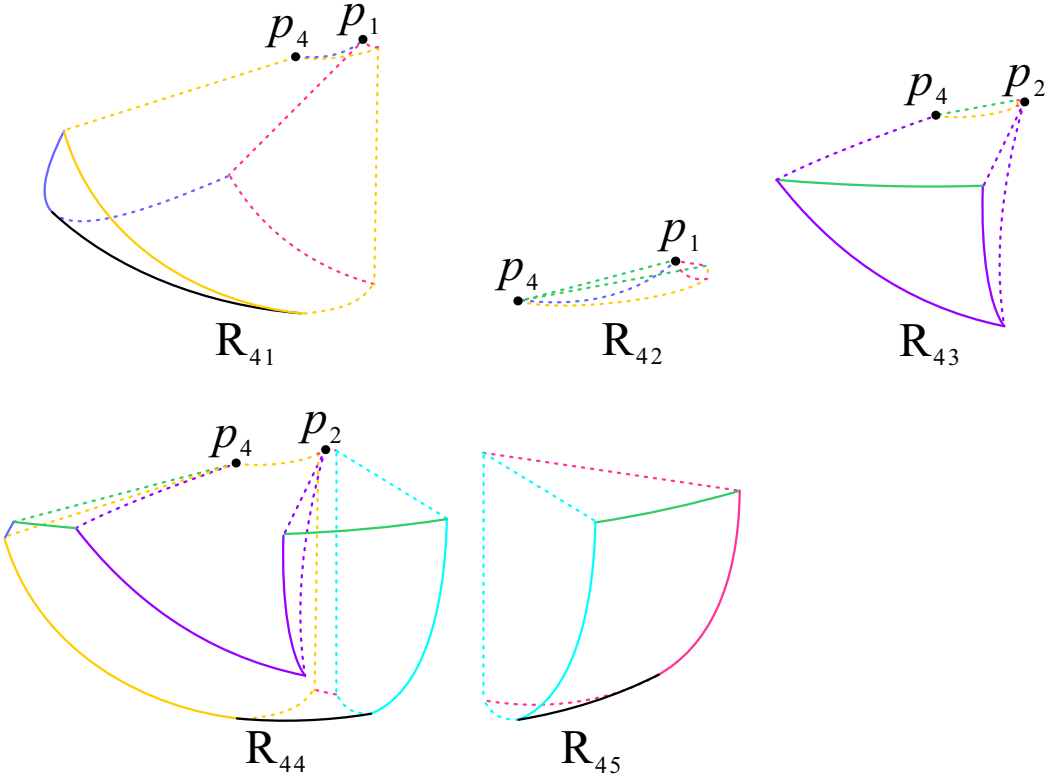

Figure 9. The region R_4 is divided into five subregions by the five planes $y = 0$, $z = 0$, $\Omega^{(m)} = 0$, $b_2 = 0$, and $b_3 = 0$, and one surface $b_1 = 0$.

For subregion R_{41}, its front part is limited by $b_2 = 0$, its back is bounded by $y = 0$ and $\Omega^{(m)} = 0$, and its bottom and top are restricted by Poincaré sphere and $b_3 = 0$, respectively. The trajectories in subregion R_{41} are monotone increasing in the positive x axis, and decreasing in the positive y and z axes. So these trajectories stem from subregions R_{42} and R_{44} and destine for the infinite equilibrium points in $y = 0$ limited to R_{41}.

The front of subregion R_{42} is restricted by $b_2 = 0$, the back is bounded by $y = 0$ and $\Omega^{(m)} = 0$, the top is confined by $z = 0$, and the bottom is limited by $b_3 = 0$. The dynamic

behavior of the trajectories in R_{42} is monotonically decreasing in the positive three axes directions. Hence, the trajectories in R_{42} stem from p_4, then leave for R_{41} and R_{43}.

For R_{43}, its top portion is limited by $z = 0$, its back is restricted by b_2 and $y = 0$, and the other portions are confined by $b_3 = 0$. The trajectories in R_{43} are monotone decreasing in the positive x and z axes, increasing in the positive y axis. These trajectories are from R_{42} and p_2, then head for R_{44}.

Table 5. Dynamic behavior of the trajectories in the five subregions.

Subregion	Corresponding Region	Dynamic Behavior
R_{21}	$b_1 > 0, b_2 < 0, b_3 > 0, y > 0, z < 0$	$\dot{x} > 0, \dot{y} < 0, \dot{z} < 0$
R_{22}	$b_1 < 0, b_2 < 0, b_3 > 0, y > 0, z < 0$	$\dot{x} < 0, \dot{y} < 0, \dot{z} < 0$
R_{23}	$b_1 < 0, b_2 > 0, b_3 > 0, y > 0, z < 0$	$\dot{x} < 0, \dot{y} > 0, \dot{z} < 0$
R_{24}	$b_1 > 0, b_2 > 0, b_3 > 0, y > 0, z < 0$	$\dot{x} > 0, \dot{y} > 0, \dot{z} < 0$
R_{25}	$b_1 > 0, b_2 > 0, b_3 < 0, y > 0, z < 0$	$\dot{x} > 0, \dot{y} > 0, \dot{z} > 0$

The top portion of subregion R_{44} is restricted by $z = 0$, b_1 and $\Omega^{(m)} = 0$, the right, left, front, and back are bounded by $b_3 = 0$, $b_2 = 0$, the Poincaré sphere, and $y = 0$, respectively. The tendency of the trajectories in R_{44} shows monotone increasing in the positive x and y axes, monotone decreasing in the positive z axis. Thus, the trajectories in R_{44} stem from p_2, p_4, R_{43}, and R_{45}, and enter R_{41}.

For subregion R_{45}, its top is confined by the plane $z = 0$, its front is limited by $b_3 = 0$ and the Poincaré sphere, and its back is restricted by $y = 0$. In R_{45}, the trajectories are monotone increasing in the positive three axes, hence they come from the infinite equilibrium points in $y = 0$ restricted to R_{45}, then get into R_{44}.

The analysis of the dynamic behavior in the five subregions presented above can be summarized as follows:

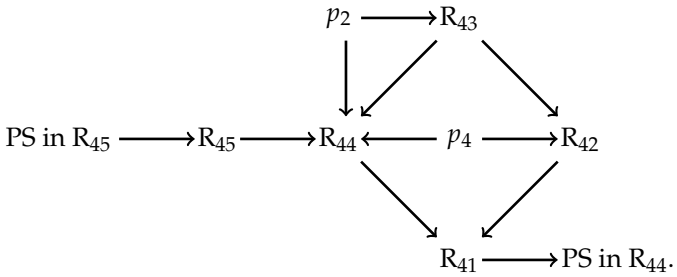

From the dynamic flow chart above, we can obtain that the trajectories in R_4 own ω-limits at the infinite equilibrium points in $y = 0$ restricted to R_{41} and α-limits at p_2, p_4, and the infinite equilibrium points in $y = 0$ restricted to R_{45}. No cosmological solution exists in R_4 because matter points and accelerated points are not located in this region.

4. Conclusions

Dynamic system analysis is a useful mathematical tool to explore the qualitative dynamic behavior of cosmological models. Due to the fact that field equations in the cosmological model include highly nonlinear terms, it is not easy to directly compare the models with the observed values. However, we can use dynamic system analysis to find the equilibrium points related to the model and the properties of these points. Since these points represent the Universe's evolution stage, we can compare the analysis of these points with observational cosmology to obtain the rationality of the model.

In minimally coupled $f(R, T)$ gravity, the function $h(T)$ is confined to a specific form $c_1\sqrt{-T} + c_2$, where c_1, c_2 are constants. Based on Case A in Section IV of [49], we choose this particular form of $f(R, T)$ gravity, which can reduce the independent variable. Considering

the late-time behavior of the model, we obtain the autonomous dynamic system with only three independent variables, which can describe the three-dimensional dynamic behavior of the system.

Through dynamic system analysis, the dynamics of the model under the background of $f(R,T) = \xi R^{\alpha} + \zeta\sqrt{-T}$ gravity in regions restricted by the three invariant planes is presented. Note that the cosmological solutions can be found in this model when α tends to 1 from the side greater than 1 (i.e., $\alpha \to 1^{+}$) [57], so we investigated the dynamic behavior of the system in three-dimensional space when the α is close to 1. As the equilibrium points p_5, p_6 are matter point and accelerated point, respectively, based on their values of $\omega^{(\mathrm{eff})}$ and $\Omega^{(\mathrm{m})}$, the evolution from p_5 to p_6 can describe a matter-dominated phase to an accelerated expansion. Thus, the evolution trajectories originating from p_5 moving to p_6 present a class of cosmological solutions. A Poincaré ball, which stands for the whole space, is divided into eight regions by the three invariant planes. However, as cosmological solutions hold when $\Omega^{(\mathrm{m})} \geq 0$, we mainly discussed the dynamic behavior of the four regions R_i $(i = 1,2,3,4)$ in three-dimensional space and discarded the analysis of the regions R_i $(i = 5,6,7,8)$ with $\Omega^{(\mathrm{m})} < 0$. The dynamic behavior of each subregion in the four regions R_i $(i = 1,2,3,4)$ is presented in Tables 2–5 and the dynamic process of all subregions are shown in the form of flow charts. The existence of cosmological solutions in the four regions has been discussed and only the region R_1 has cosmological solutions which can represent the evolution from the matter-dominated epoch to the accelerated expansion.

Author Contributions: Conceptualization, F.G.; formal analysis, J.L. and R.W.; software, J.L.; writing—original draft, J.L.; writing—review and editing, F.G. All authors have read and agreed to the published version of the manuscript.

Funding: This research was funded by the National Natural Science Foundation of China (NSFC) through grant Nos. 12172322 and 11672259, the "High-end Talent Support Program" of Yangzhou University, and the Postgraduate Research & Practice Innovation Program of Jiangsu Province (KYCX21_3190).

Institutional Review Board Statement: Not applicable.

Informed Consent Statement: Not applicable.

Data Availability Statement: Not applicable.

Conflicts of Interest: The authors declare no conflict of interest.

References

1. de Bernardis, P.; Ade, P.A.R.; Bock, J.J.; Bond, J.R.; Borrill, J.; Boscaleri, A.; Coble, K.; Crill, B.P.; Gasperis, G.D.; Farese, P.C.; et al. A flat Universe from high-resolution maps of the cosmic microwave background radiation. *Nature* **2000**, *404*, 955–959. [CrossRef]
2. Bennett, B.C.L.; Hill, R.S.; Hinshaw, G.; Nolta, M.R.; Odegard, N.; Page, L.; Spergel, D.N.; Weiland, J.L.; Wright, E.L.; Halpern, M.; et al. First-year wilkinson microwave anisotropy probe (WMAP)* observations: Foreground emission. *Astrophys. J. Suppl. Ser.* **2003**, *148*, 97. [CrossRef]
3. Spergel, D.N.; Verde, L.; Peiris, H.V.; Komatsu, E.; Nolta, M.R.; Bennett, C.L.; Halpern, M.; Hinshaw, G.; Jarosik, N.; Kogut, A.; et al. First-year Wilkinson Microwave Anisotropy Probe (WMAP)* observations: Determination of cosmological parameters. *Astrophys. J. Suppl. Ser.* **2003**, *148*, 175. [CrossRef]
4. Riess, A.G.; Filippenko, A.V.; Challis, P.; Clocchiatti, A.; Diercks, A.; Garnavich, P.M.; Gilliland, R.L.; Hogan, C.J.; Jha, S.; Kirshner, R.P.; et al. Observational evidence from supernovae for an accelerating universe and a cosmological constant. *Astron. J.* **1998**, *116*, 1009. [CrossRef]
5. Bennett, C.L.; Bay, M.; Halpern, M.; Hinshaw, G.; Jackson, C.; Jarosik, N.; Kogut, A.; Limon, M.; Meyer, S.S.; Page, L.; et al. The microwave anisotropy probe* mission. *Astrophys. J.* **2003**, *583*, 1. [CrossRef]
6. Peeebles, P.J.E. Probing general relativity on the scales of cosmology. *Gen. Relativ. Gravit.* **2005**, 106–117.
7. Cai, Y.F.; Saridakis, E.N.; Setare, M.R.; Xia, J.-Q. Quintom cosmology: Theoretical implications and observations. *Phys. Rep.* **2010**, *493*, 1–60. [CrossRef]
8. Copeland, E.J.; Sami, M.; Tsujikawa, S. Dynamics of dark energy. *Int. J. Mod. Phys. D* **2006**, *15*, 1753–1935. [CrossRef]
9. Errehymy, A.; Daoud, M. Studies an analytic model of a spherically symmetric compact object in Einsteinian gravity. *Eur. Phys. J. C* **2020**, *80*, 1–12. [CrossRef]
10. Sotiriou, T.P.; Faraoni, V. $f(R)$ theories of gravity *Rev. Mod. Phys.* **2010**, *82*, 451. [CrossRef]

11. De Felice, A.; Tsujikawa, S. $f(R)$ Theories. *Living. Rev. Relativ.* **2010**, *13*, 1–161. [CrossRef]
12. Cai, Y.F.; Capozziello, S.; De Laurentis, M.; Saridakis, E N. $f(T)$ teleparallel gravity and cosmology. *Rep. Prog. Phys.* **2016**, 79, 106901. [CrossRef]
13. Nojiri, S.I.; Odintsov, S.D. Modified Gauss–Bonnet theory as gravitational alternative for dark energy. *Phys. Lett. B* **2005**, *631*, 1–6. [CrossRef]
14. Nojiri, S.I.; Odintsov, S.D.; Gorbunova, O.G. Dark energy problem: from phantom theory to modified Gauss–Bonnet gravity. *J. Phys. A Math. Gen.* **2006**, *39*, 6627. [CrossRef]
15. Harko, T.; Lobo, F.S.; Nojiri, S.I.; Odintsov, S.D. $f(R,T)$ gravity. *Phys. Rev. D* **2011**, *84*, 024020. [CrossRef]
16. Harko, T.; Lobo, F.S.; Otalora, G.; Saridakis, E.N. $f(T,\mathcal{T})$ gravity and cosmology. *J. Cosmol. Astropart. Phys.* **2014**, *2014*, 021. [CrossRef]
17. Starobinsky, A.A. Disappearing cosmological constant in $f(R)$ gravity. *JETP. Lett.* **2007**, *86*, 157–163. [CrossRef]
18. Tsujikawa, S. Observational signatures of $f(R)$ dark energy models that satisfy cosmological and local gravity constraints. *Phys. Rev. D* **2007**, *77*, 023507. [CrossRef]
19. Nojiri, S.I.; Odintsov, S.D.; Sáez-Gómez, D. Cosmological reconstruction of realistic modified $f(R)$ gravities. *Phys. Lett. B* **2009**, *681*, 74–80. [CrossRef]
20. Nojiri, S.I.; Odintsov, S.D.; Oikonomou, V.K. Unifying inflation with early and late-time dark energy in $f(R)$ gravity. *Phys. Dark Universe* **2020**, *29*, 100602. [CrossRef]
21. Bamba, K.; Odintsov, S.D. Inflationary cosmology in modified gravity theories. *Symmetry* **2015**, *7*, 220–240. [CrossRef]
22. Sebastiani, L.; Myrzakulov, R. F(R)-gravity and inflation. *Int. J. Geom. Methods Mod. Phys.* **2015**, *12*, 1530003. [CrossRef]
23. Olmo, G.J.; Rubiera-Garcia, D. Junction conditions in Palatini $f(R)$ gravity. *Class. Quantum Gravity* **2020**, *37*, 215002. [CrossRef]
24. Capozziello, S.; Mantica, C.A.; Molinari, L.G. Cosmological perfect-fluids in $f(R)$ gravity. *Int. J. Geom. Methods Mod. Phys.* **2019**, *16*, 1950008. [CrossRef]
25. Nojiri, S.; Odintsov, S.D.; Oikonomou, V.K. Modified gravity theories on a nutshell: Inflation, bounce and late-time evolution. *Phys. Rept.* **2017**, *692*, 1–104. [CrossRef]
26. Oikonomou, V.K. Unifying of inflation with early and late dark energy epochs in axion $f(R)$ gravity. *Phys. Rev. D* **2021**, *103*, 044036. [CrossRef]
27. Arora, S.; Mandal, S.; Chakraborty, S.; Leon, G.; Sahoo, P.K. Can $f(R)$ gravity isotropise a pre-bounce contracting universe? *J. Cosmol. Astropart. Phys.* **2022**, *2022*, 042. [CrossRef]
28. Sharif, M.; Zubair, M. Thermodynamics in $f(R,T)$ theory of gravity. *J. Cosmol. Astropart. Phys.* **2012**, *2012*, 028. [CrossRef]
29. Houndjo, M.J.S.; Alvarenga, F.G.; Rodrigues, M.E.; Jardim, D.F.; Myrzakulov, R. Thermodynamics in Little Rip cosmology in the framework of a type of $f(R,T)$ gravity. *Eur. Phys. J. Plus* **2014**, *129*, 1–12. [CrossRef]
30. Bhattacharjee, S.; Sahoo, P.K. Redshift drift in $f(R,T)$ gravity. *New Astron.* **2020**, *81*, 101425. [CrossRef]
31. Moraes, P.H.R.S.; Sahoo, P.K. Nonexotic matter wormholes in a trace of the energy-momentum tensor squared gravity. *Phys. Rev. D* **2018**, *57*, 024007. [CrossRef]
32. Bhatti, M.Z.; Yousaf, Z.; Ilyas, M. Existence of wormhole solutions and energy conditions in $f(R,T)$ gravity. *J. Astrophys.* **2018**, *39*, 1–11. [CrossRef]
33. Alves, M.E.S.; Moraes, P.H.R.S.; De Araujo, J.C.N.; Malheiro, M. Gravitational waves in $f(R,T)$ and $f(R,T\phi)$ theories of gravity. *Phys. Rev. D* **2016**, *94*, 024032. [CrossRef]
34. Sharif, M.; Siddiqa, A. Propagation of polar gravitational waves in $f(R,T)$ scenario. *Gen. Relativ. Gravit.* **2019**, *51*, 74. [CrossRef]
35. Sahoo, P.K.; Bhattacharjee, S. Gravitational baryogenesis in non-minimal coupled $f(R,T)$ gravity. *Int. J. Theor. Phys.* **2020**, *59*, 1451–1459. [CrossRef]
36. Shamir, M.F.; Jhangeer, A.; Bhatti, A.A. Exact solutions of Bianchi types I and V models in $f(R,T)$ gravity. *arXiv* **2012** arXiv:1207.0708.
37. Alvarenga, F.G.; De La Cruz-Dombriz, A.; Houndjo, M.J.S.; Rodrigues, M.E.; Sáez-Gómez, D. Dynamics of scalar perturbations in $f(R,T)$ gravity. *Phys. Rev. D* **2013**, *87*, 103526. [CrossRef]
38. Bhattacharjee, S.; Sahoo, P.K. Big bang nucleosynthesis and entropy evolution in $f(R,T)$ gravity. *Eur. Phys. J. Plus* **2020**, *135*, 1–10. [CrossRef]
39. Azmat, H.; Zubair, M. An anisotropic version of Tolman VII solution in $f(R,T)$ gravity via gravitational decoupling MGD approach. *Eur. Phys. J. Plus* **2021**, *136*, 1–17. [CrossRef]
40. Shaikh, A.Y. Panorama behaviors of general relativistic hydrodynamics and holographic dark energy in $f(R,T)$ gravity. *New Astron.* **2022**, *91*, 101676. [CrossRef]
41. Gashti, S.N.; Sadeghi, J.; Upadhyay, S.; Alipour, M.R. Swampland dS conjecture in mimetic $f(R,T)$ gravity. *Commun. Theor. Phys.* **2022**, *74*, 085402. [CrossRef]
42. Gonçalves, T.B.; Rosa, J.L.; Lobo, F.S. Cosmology in scalar-tensor $f(R,T)$ gravity. *Phys. Rev. D* **2022**, *105*, 064019. [CrossRef]
43. Santos, A.F. Gödel solution in $f(R,T)$ gravity. *Mod. Phys. Lett. A* **2013**, *28*, 1350141. [CrossRef]
44. Bhatti, M.Z.; Yousaf, Z.; Yousaf, M. Stability of self-gravitating anisotropic fluids in $f(R,T)$ gravity. *Phys. Dark Universe* **2020**, *28*, 100501. [CrossRef]
45. Sharif, M.; Zubair, M. Cosmological reconstruction and stability in $f(R,T)$ gravity. *Gen. Relativ. Gravit.* **2014**, *46*, 1723. [CrossRef]

46. Singh, C.P.; Singh, V. Reconstruction of modified $f(R,T)$ gravity with perfect fluid cosmological models. *Gen. Relativ. Gravit.* **2014**, *46*, 1696. [CrossRef]
47. Azmat, H.; Zubair, M.; Ahmad, Z. Study of anisotropic and non-uniform gravastars by gravitational decoupling in $f(R,T)$ gravity. *Ann. Phys.* **2022**, *439*, 168769. [CrossRef]
48. Koussour, M.; Bennai, M. On a Bianchi type-I space-time with bulk viscosity in $f(R,T)$ gravity. *Int. J. Geom. Methods Mod. Phys.* **2022**, *19*, 2250038. [CrossRef]
49. Shabani, H.; Farhoudi, M. $f(R,T)$ cosmological models in phase space. *Phys. Rev. D* **2013**, *88*, 044048. [CrossRef]
50. Guo, J.Q.; Frolov, A.V. Cosmological dynamics in $f(R)$ gravity. *Phys. Rev. D* **2013**, *88*, 124036. [CrossRef]
51. Zonunmawia, H; Khyllep, W; Dutta, J; Järv, L. Cosmological dynamics of brane gravity: A grobal dynamical system perspective. *Phys. Rev. D* **2018**, *98*, 083532. [CrossRef]
52. Singh, A.; Singh, G.P.; Pradhan A. Cosmic dynamics and qualitative study of Rastall model with spatial curvature. *Int. J. Mod. Phys. A* **2022**, *37*, 2250104. [CrossRef]
53. Gao, F.B.; Llibre, J. Global dynamics of the Hořava-Lifshitz cosmological system. *Gen. Relativ. Gravit.* **2019**, *51*, 152. [CrossRef]
54. Gao, F.B.; Llibre, J. Global dynamics of Hořava-Lifshitz cosmology with non-zero curvature and a wide range of potentials. *Eur. Phys. J. C* **2020**, *80*, 137. [CrossRef]
55. Gao, F.B.; Llibre, J. Global dynamics of the Hořava-Lifshitz cosmological model in a non-flat universe with non-zero cosmological constant. *Universe* **2021**, *7*, 445. [CrossRef]
56. Gao, F.B.; Llibre, J. Global dynamics of the Hořava-Lifshitz cosmology in the presence of non-zero cosmological constant in a flat space. *Phys. Dark Universe* **2022**, *38*, 101139. [CrossRef]
57. Liu, J.W.; Wang, R.F.; Gao, F.B. Dynamics of a cosmological model in $f(R,T)$ gravity: I. on invariant planes. *Universe* **2022**, *8*, 365. [CrossRef]
58. Amendola, L. Coupled quintessence. *Phys. Rev. D* **2000**, *62*, 043511. [CrossRef]
59. Dumortier, F.; Llibre, J.; Ateés, J.C. *Qualitative Theory of Planar Differential Systems*; Springer: Berlin/Heidelberg, Germany, 2006.